

# Development of a SiYAION Glaze for Improved Osteoconductivity of Implantable Medical Devices

Ryan M. Bock,<sup>1</sup> Elia Marin,<sup>2</sup> Alfredo Rondinella,<sup>2,3</sup> Francesco Boschetto,<sup>2,3</sup> Tetsuya Adachi,<sup>3,4</sup> Bryan J. McEntire ,<sup>1</sup> B. Sonny Bal,<sup>1,5</sup> Giuseppe Pezzotti<sup>2</sup>

<sup>1</sup>Amedica Corporation, Salt Lake City, Utah 84119

<sup>2</sup>Ceramic Physics Laboratory, Kyoto Institute of Technology, Sakyo-ku, Matsugasaki, 606-8126 Kyoto, Japan

<sup>3</sup>Department of Dental Medicine, Kyoto Prefectural University of Medicine, Kawaramachi Hirokoji, Kamigyo-ku, 602-8566 Kyoto, Japan

<sup>4</sup>Department of Immunology, Kyoto Prefectural University of Medicine, Kawaramachi Hirokoji, Kamigyo-ku, 602-8566 Kyoto, Japan

<sup>5</sup>Department of Orthopaedic Surgery, University of Missouri, Columbia, Missouri 65212

Received 16 November 2016; revised 11 April 2017; accepted 22 April 2017

Published online 00 Month 2017 in Wiley Online Library (wileyonlinelibrary.com). DOI: 10.1002/jbm.b.33914

**Abstract:** The application of bioactive coatings onto orthopaedic appliances is commonly performed to compensate for the otherwise bioinert nature of medical devices and to improve their osseointegration. Calcium phosphates, hydroxyapatite (HAp), and bioglasses are commercially available for this purpose. Until recently, few other inorganic compounds have been identified with similar biofunctionality. However, silicon nitride ( $\text{Si}_3\text{N}_4$ ) has emerged as a new orthopaedic material whose unique surface chemistry also enhances osteoconductivity. Recent research has confirmed that its minority intergranular phase, consisting of silicon yttrium aluminum oxynitride (SiYAION), is principally responsible for this improvement. As a result, it was hypothesized that SiYAION itself might serve as an effective osteoconductive coating or glaze for medical devices. To test this hypothesis, a process inspired by traditional ceramic whiteware glazing was developed. A slurry containing ingredients similar to the

intergranular SiYAION composition was applied to a  $\text{Si}_3\text{N}_4$  surface, which was then subjected to a heat treatment to form a glaze. Various analytical tools were employed to assess its chemistry and morphology. It was found that the glaze was comprised predominately of  $\text{Y}_5\text{Si}_3\text{O}_{12}\text{N}$ , a compound commonly referred to as N-apatite, which is isostructural to native HAp. Subsequent exposure of the glazed surface to acellular simulated body fluid led to increased deposition of biomimetic HAp-like crystals, while exposure to Saos-2 osteosarcoma cells *in vitro* resulted in greater HAp deposition relative to control samples. The observation that SiYAION exhibits enhanced osteoconductivity portends its potential as a therapeutic aid in bone and tissue repair. © 2017 Wiley Periodicals, Inc. *J Biomed Mater Res Part B: Appl Biomater* 00B: 000–000, 2017.

**Key Words:** silicon nitride, SiYAION, bioceramics, orthopedic implants, osteosarcoma

**How to cite this article:** Bock RM, Marin E, Rondinella A, Boschetto F, Adachi T, McEntire BJ, Bal BS, Pezzotti G. 2017. Development of a SiYAION Glaze for Improved Osteoconductivity of Implantable Medical Devices. *J Biomed Mater Res Part B* 2017;00B:000–000.

## INTRODUCTION

Beyond restoring bodily function, the goal of every alloplastic medical device is its rigid and permanent integration with musculoskeletal tissue. This is particularly crucial for large weight-bearing implants such as spinal arthrodesis devices and total hip or knee arthroplasty systems. Over the past 50 years significant advancements in implant design and biomaterials have occurred, including the development of coatings and composites containing bioactive constituents such as calcium phosphates (CaP), synthetic hydroxyapatite (HAp), and bioglasses.<sup>1–3</sup> Yet, despite these valued efforts, aseptic loosening remains as the leading cause for revision surgery, requiring the removal of poorly fixated implants.<sup>4,5</sup> Clearly, there is a continued need for new and novel

materials to improve the osseointegration of biomedical devices. However, other than CaP-based ceramics and bioactive glasses, few inorganic materials have similar biofunctionality.

A relatively recent addition to this list is silicon nitride ( $\text{Si}_3\text{N}_4$ ),<sup>6</sup> a nonoxide material that possesses ideal properties for use in orthopedic applications.<sup>7–11</sup> It is prepared as a two-phase composite composed of interlocking anisotropic  $\text{Si}_3\text{N}_4$  grains separated by a thin continuous intergranular phase (IGP) of silicon yttrium aluminum oxynitride (SiYAION). Dense monolithic  $\text{Si}_3\text{N}_4$  exhibits a favorable combination of wear resistance, flexural strength, and fracture toughness.<sup>12–15</sup> However,  $\text{Si}_3\text{N}_4$  can also be formed as a highly porous construct, ideal for use in bone scaffolds and

**Correspondence to:** R. M. Bock; e-mail: rbock@amedica.com

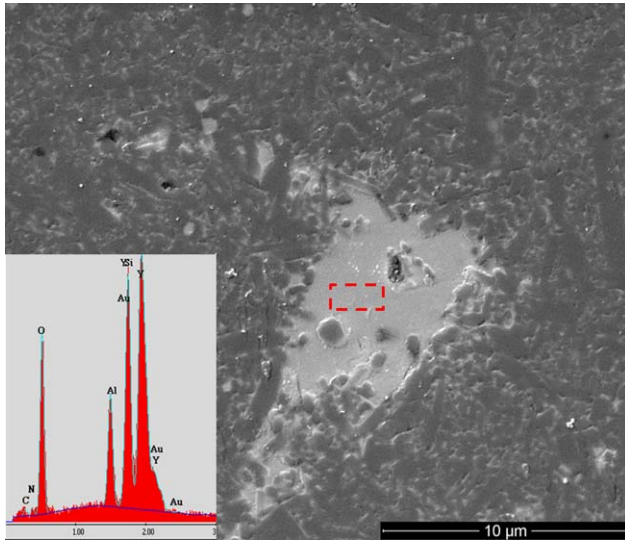


**FIGURE 1.** Back-scattered electron micrograph of cross-sectioned and polished  $\text{Si}_3\text{N}_4$  component showing pooled IGP filling bulk defect and associated EDS spectrum (inset, bottom-left). Box drawn on micrograph indicates area of EDS scan.

arthrodesis devices.<sup>16–18</sup> It is biocompatible,<sup>19–25</sup> partially radiolucent,<sup>10,26,27</sup> integrates well with bone,<sup>6,28,29</sup> and provides intrinsic resistance to bacterial colonization<sup>30–32</sup> when compared to polyetheretherketone (PEEK) and titanium.<sup>28,31</sup>  $\text{Si}_3\text{N}_4$  was first used as a spinal implant in a small clinical trial in Australia in 1986.<sup>23</sup> Since 2008, it has been routinely used for spinal fusion cages, with >30,000 implantations to date and few reported adverse events.<sup>33</sup>

Previous efforts demonstrated that the concentrations of  $\equiv\text{Si}-\text{OH}$  and  $\equiv\text{Si}-\text{NH}_2$  functional groups at the surface of  $\text{Si}_3\text{N}_4$  could be tuned by subjecting the material to chemical etch treatments and controlled atmosphere annealing cycles.<sup>34</sup> These treatments were shown to disrupt the native  $\text{Si}_2\text{N}_2\text{O}$  passivation layer by either stripping it away to expose the underlying  $\text{Si}_3\text{N}_4$  grains (viz., by HF etching) or further oxidizing it to produce an amorphous  $\text{SiO}_2$  layer (viz., by annealing in air). Relevant biomaterial properties, such as hydrophilicity and surface charging, were strongly influenced by manipulating  $\text{Si}_3\text{N}_4$ 's surface in this manner. It was further demonstrated that annealing  $\text{Si}_3\text{N}_4$  in a nitrogen atmosphere caused a portion of its minority SiYAlON IGP to exude from the ceramic and form small discrete islands on its surface, effectively forming a partial glaze. Surprisingly, it was discovered that the presence of this intermittent glaze gave the surface superhydrophilic behavior (that is, a static water

contact angle  $<10^\circ$ ) and a robust net negative surface charge at physiologic pH.<sup>34</sup> A subsequent *in vitro* study used Saos-2 osteosarcoma cells to assess this surface's osteoconductivity potential and demonstrated that cell density and osteoid mineralization were both maximized on the discrete SiYAlON precipitates. Further, when osteoid mineralization was prevented by exclusion of ascorbic acid from the culture medium, preferential cell clustering on these SiYAlON islands was still observed.<sup>6</sup> In light of these results, it was hypothesized that the SiYAlON glaze itself might be a potential new and novel bioactive glass. It was further postulated that the use of SiYAlON, either as a coating or glaze, on an implantable biomaterial might lead to enhanced eukaryotic cell responsiveness and improved osseointegration.

Consequently, the primary objectives of this study were twofold: (1) Demonstrate that a SiYAlON glaze can be applied to an implantable biomaterial's surface; and (2) Characterize the glaze in terms of its morphology, chemistry, and potential for enhanced osteoconductivity. To achieve the first objective, a process inspired by traditional ceramic whiteware glazing was developed. For simplicity,  $\text{Si}_3\text{N}_4$  was selected as the implantable biomaterial. An aqueous slurry containing the SiYAlON ingredients (as a frit) was applied to this  $\text{Si}_3\text{N}_4$  substrate and subsequently fired to form a glaze. The glaze was then extensively characterized using various microscopic and spectroscopic techniques. The potential for enhanced osteoconductivity was subsequently evaluated using two *in vitro* methods. First, the glaze's affinity for apatite formation and deposition was determined using an *in vitro* acellular ISO protocol.<sup>35</sup> Second, Saos-2 osteosarcoma cell adsorption, proliferation, osteoid deposition, and HAP formation were examined using a previously validated procedure.<sup>29</sup>

## MATERIALS AND METHODS

### SiYAlON glaze preparation

The selected composition of the SiYAlON glaze was experimentally determined from an EDS analysis of a glass filled defect on a polished cross-section of a  $\text{Si}_3\text{N}_4$  component as shown in Figure 1, with the specific elemental ratios given in Table I. This component was prepared in accordance with standard manufacturing practices described elsewhere.<sup>36</sup> After determining the composition, a glass frit was prepared by mixing silica ( $\text{SiO}_2$ , 0.5  $\mu\text{m}$ , Alfa Aesar, Ward Hill, MA), yttria ( $\text{Y}_2\text{O}_3$ , Grade C, H. C. Starck, Munich, Germany), aluminum nitride (AlN, Grade C, H. C. Starck, Munich, Germany), theta-alumina ( $\theta\text{-Al}_2\text{O}_3$ , APA-0.2, Sasol, Houston, TX), and  $\text{Si}_3\text{N}_4$  (Ube SN-E10, Ube City, Japan) in deionized

**TABLE I. Designed Elemental and Molecular Compositions of SiYAlON Glazing Slurry**

Element	IGP Composition (at.%)	SiYAlON Slurry (at.%)	Compound	SiYAlON Slurry (mol %)
Si	20.81%	15.6%	$\text{SiO}_2$	48.8%
Y	20.81%	15.6%	$\text{Y}_2\text{O}_3$	28.0%
Al	9.50%	7.1%	AlN	16.0%
O	44.34%	54.6%	$\text{Al}_2\text{O}_3$	4.8%
N	4.52%	7.1%	$\text{Si}_3\text{N}_4$	2.4%

Observed elemental composition of IGP via EDS is included for comparison.

water at 5 volume % (vol %) solids. Citric acid (Sigma-Aldrich Corp., St. Louis, MO) was employed as a dispersant at 1 weight % (wt %) of solids, and ammonium hydroxide (Sigma-Aldrich Corp., St. Louis, MO) was added in sufficient quantity to increase the pH of the slurry to 10. The slurry was rolled on a laboratory jar mill (U.S. Stoneware, East Palestine, OH) for about 18 h within a polypropylene jar using Si<sub>3</sub>N<sub>4</sub> milling media (Ø5 mm spheres, St. Gobain North America, Malvern, PA) to facilitate mixing and the breakdown of soft agglomerates. After milling, the slurry was diluted to 0.25 vol % solids and ammonium bicarbonate (NH<sub>4</sub>HCO<sub>3</sub>, Sigma-Aldrich Corp., St. Louis, MO) was added at a concentration of 0.1 mol/L of water to facilitate particle rearrangement during drying.<sup>37</sup> Finally, the diluted slurry was equilibrated by rolling it on the mill for a minimum of 2 h prior to being used for glazing.

The diluted SiYALON slurry was then applied to Si<sub>3</sub>N<sub>4</sub> biomaterial discs (Ø12.7 × 3 mm<sup>2</sup>) using a dip-coating technique. Processing of the discs was in accordance with standard commercial manufacturing methods.<sup>36</sup> The discs were used in their “as-fabricated” (AFSN) state, meaning that they were not subjected to any post densification machining operations. Each disc was coated by gripping its edges with stainless steel tweezers, immersing it into the slurry, and then slowly withdrawing it. Each coated disc was then placed into an acrylic desiccator cabinet (Ted Pella, Redding, CA) containing hygroscopic media (Indicating Drierite, W.A. Hammond DRIERITE Co., Xenia, OH) for a minimum of 2 h for drying. Following initial drying, the samples were placed in a drying oven (Binder, Bohemia, NY) and held at 90°C for at least 2 h to further facilitate drying and decomposition of the NH<sub>4</sub>HCO<sub>3</sub> additive. After this heated drying step, the slurry-coated samples were placed in a batch furnace (Model 121224, Centorr Vacuum Industries, Nashua, NH), evacuated to 250 mTorr, then back-filled with filtered N<sub>2</sub> (1–2 psi), and subsequently heated to 1400°C for 30 min to form the fired glaze.<sup>34</sup>

### SiYALON glaze characterization

Scanning Electron Microscopy (SEM) and Energy Dispersive X-Ray Spectroscopy (EDS) – SEM was carried out using a field emission gun scanning electron microscope (FEG-SEM, Quanta, FEI, Hillsboro, OR). All samples were sputter-coated with a thin (~20–30 Å) layer of gold (108auto, Cressington, Watford, UK) or gold-palladium (Model 682 Precision Etching Coating System, Gatan, Pleasanton, CA). Samples were typically imaged using an accelerating voltage of 10 kV at working distances of 7–10 mm and a spot size of 4.5 mm. EDS was performed simultaneously while imaging using a spectrometer (EDAX, Mahwah, NJ) attached to the SEM. Quantitative compositional analysis of the EDS spectrum was acquired using commercial software (EDAX Genesis, EDAX, Mahwah, NJ) which employed matrix corrections for atomic number, absorption, and fluorescence (ZAF matrix correction).

**X-Ray Photoelectron Spectroscopy (XPS).** A spectrometer (Axis Ultra, Kratos, Manchester, UK) was employed with an

Al K $\alpha$  monochromatic X-ray source. Low-resolution spectral scans were conducted using a pass energy of 160 eV, with a compositional resolution of ~0.1 atomic percent (at.%). High resolution scans bracketing peaks of interest were conducted using a pass energy of 40 eV, which was expected to improve the compositional resolution to approximately 0.01 at.%. The analysis area was set to 700 × 300  $\mu\text{m}^2$  to average the polyphasic surface’s compositional heterogeneity. Data obtained were processed using commercially available software (CasaXPS, Casa Software, UK). Charging effects were mitigated using a low energy electron source and application of ultrahigh vacuum-rated colloidal silver (Ted Pella, Redding, CA) to the contact points between the samples and the fixture. All reported data were obtained following argon sputtering to remove adsorbed surface contaminants, at a beam energy of 4.2 keV, gun angle with respect to sample of 45°, raster area of 3 × 3 mm<sup>2</sup>, and a sample current of ~2  $\mu\text{A}$ .

**X-Ray Diffraction (XRD).** Samples were examined using an X-ray diffractometer (Panalytical X’Pert MPD, Philips, Almelo, The Netherlands) with instrument and program settings as follows: Voltage: 45 kV, Current: 40 mA, Divergence Slit: 1/2 degree, Anti-Scatter Slit: 1/4 degree, Receiving Slit: 1/8 degree, Scan range: 20–70° 2 $\theta$ , Step Size: 0.015° at a rate of 1.5 s/step. Specimens were analyzed using commercial software (X’Pert Highscore Plus, Philips, Almelo, The Netherlands). Raw data were first treated by searching for peaks and determining background. The resulting patterns were then matched with ICDD/ICSD database reference patterns after applying elemental database restrictions. The database search provided a list of reference patterns with a match score, indicating each pattern’s overlap with peak intensity and position in the experimental spectrum. The phases were matched based on scoring from the software, reference pattern quality, and qualitative analysis.

**Raman Spectroscopy.** Raman spectra were acquired from the inorganic samples using a confocal (optical) microprobe at room temperature and a single monochromator (T-64000, Jobin-Yvon/Horiba Group, Kyoto, Japan) equipped with a nitrogen-cooled 1024 × 256 pixels CCD camera (CCD-3500 V, Horiba Ltd., Kyoto, Japan), and analyzed by using commercially available software (LabSpec, Horiba/Jobin-Yvon, Kyoto, Japan). The excitation frequency used in the experiment was the 532 nm blue line of an Ar-ion laser operating at a power of 100 mW. The spectrum integration time was typically 30 s, averaging the recorded spectra over three successive measurements. A confocal configuration of the Raman probe was adopted throughout all of the experiments using a 100× objective lens to exclude the photons scattered from out-of-focus regions of the probe. A signal from a He-Ne lamp was collected throughout all measurements as an internal reference for Raman peak positions. Raman band parameters were obtained by fitting the raw experimental spectra with Lorentzian curves. An additional set of Raman experiments was carried out on living cells by means of different Raman equipment and modalities, which

will be described in the next subsection together with the explanation of cell culture.

### Osteoconductivity tests

**Immersion in Simulated Body Fluid (SBF).** An *in vitro* ISO protocol was used to assess the potential for the SiYALON glaze to induce precipitation of HAp onto its surface.<sup>35</sup> Kokubo and coworkers demonstrated that immersion of prospective biomaterials in SBF per this protocol can predict osteoconductive behavior.<sup>38–47</sup> Specifically, materials that exhibit the ability to induce precipitation of biomimetic HAp from SBF via a surface charge-initiated mechanism *in vitro*<sup>48</sup> also tend to display osteoconductive<sup>49,50</sup> and potentially osseointegrative<sup>51</sup> characteristics *in vivo*. In this study, the SBF was prepared according to an established recipe (*viz.*, m-SBF) which closely approximates the ionic composition of human blood plasma.<sup>44,52</sup> The batched SBF was stored overnight at 5°C and used for experiments within 24 h. Samples were placed roughly horizontally in the conical bottoms of polypropylene tubes (50 mL, CentriStar, Corning Life Sciences, Corning, NY) which were sealed with rubber septa (self-sealing, 24/40, Ace Glass, Vineland, NJ). SBF was pumped (Variable Flow Peristaltic, Control Company, Friendswood, TX) into each tube through a needle (18 G, Nokor, BD, Franklin Lakes, NJ) via silicone tubing (0.25" I.D.) containing an inline filter (0.2 µm, Polycap TC, Whatman, Buckinghamshire, UK). The filter was employed in order to both sterilize the SBF and minimize the presence of fine particulates in solution that could act as potential heterogeneous nucleation sites. Prepared samples were then placed in a test tube rack held within a water bath (W-10, Anova, Stafford, TX) whose temperature was maintained at  $36.5 \pm 0.15^\circ\text{C}$  via a digitally controlled thermostat to conform to the established procedure.<sup>35,39</sup> The sample surfaces were faced downward during the experiment. This was done to prevent potential settling of dispersoid precipitates onto observation surfaces and skewing results. Following 28 days of immersion in the heated water bath, the tubes were removed and the samples recovered. Samples were then rinsed in a succession of three deionized water baths in order to minimize the chance of remnant SBF ions causing supplemental postexperiment precipitation on their surfaces during drying. Following recovery, samples were placed in a desiccating cabinet containing hygroscopic media for a period of at least 24 h prior to their characterization. Two sets of control samples, identical in geometry to the test samples, were subjected to the same SBF immersion test. These control discs consisted of both as-fabricated (AFSN) and nitrogen-annealed (N<sub>2</sub>ASN) Si<sub>3</sub>N<sub>4</sub>. They were selected because they had previously demonstrated enhanced osteoconductive behavior using living Saos-2 osteosarcoma cells.<sup>6,29</sup> When not being evaluated, all samples were stored in a desiccating cabinet to minimize inadvertent surface contamination.

**Osteosarcoma Cell Test.** Cells from the Saos-2 cell line were cultured in an osteogenic medium consisting of 4.5 g/L glucose DMEM (D-glucose, L-Glutamine, Phenol red, and Sodium Pyruvate) with 10% fetal bovine serum and allowed to

incubate for about 24 h at 37°C resulting in a final Saos-2 concentration of  $5 \times 10^5$  cells/mL. Cultured cells were seeded onto sample surfaces previously subjected to UV sterilization, in an osteogenic medium consisting of DMEM supplemented with 50 µg/mL ascorbic acid, 10 mM β-glycerol phosphate, 100 mM hydrocortisone, and 10% fetal bovine calf serum. The seeded samples were incubated for 7 days at 37°C and the medium was refreshed twice during that period. At the conclusion of their incubation, Raman image maps were generated with a Laser Raman Microscope (RAMANtouch, Nanophoton, Osaka, Japan) using a 20× immersion-type objective and a 532 nm wavelength laser source. Each pixel measured  $1.02 \times 1.02$  µm and each image was composed of 171 horizontal rows of 400 pixels. Two regions of the resulting spectra were used for assessment of osteoid formation and mineralization – the principal band associated with P–O stretching within PO<sub>4</sub><sup>3-</sup> tetrahedra located at  $965 \pm 12.5$  cm<sup>-1</sup>,<sup>53,54</sup> and a band indicative of C–H bond stretching within collagen located at  $2939.5 \pm 42.6$  cm<sup>-1</sup>.<sup>53,54</sup> When overlaid on each other the maps illustrate the deposition of collagen, the primary ingredient in osteosarcoma's extracellular polymer (ECP),<sup>55</sup> and the amount of HAp deposited onto the collagen matrix. This allows for qualitative and quantitative comparison of the proliferation of osteosarcoma cells and the volume of deposited apatite. Note that the spectrometer employed in living-cell experiments allowed for ultra-fast imaging with Raman maps being collected in a time faster than the movement of cells. The software attached to this equipment automatically provided average spectra on selected areas. Raman spectra from living cells active on different surfaces were compared by averaging over  $\sim 10^3$  measurements for each sample. Following the experiment, one sample from each condition was removed from the osteogenic medium and prepared for fluorescence microscopy by rinsing twice in phosphate buffered saline (PBS), fixing in 4% formaldehyde with a 15 min incubation period at room temperature, rinsing twice more in PBS, adding mouse anti-human antibody (osteocalcin; Clone2H9F11F8, Isotype IgG2a, Bio-Rad, Japan) diluted to 1% in PBS, a 30 min incubation period at room temperature, rinsing twice more in PBS, adding a mixed staining solution consisting of a 1% solution in PBS of Hoechst 33342 ( $\lambda_{\text{ex}} = 352$  nm,  $\lambda_{\text{em}} = 461$  nm, Dojindo, Japan) and 1% in PBS goat anti-mouse antibody anti-igG FITC conjugate ( $\lambda_{\text{ex}} = 490$  nm,  $\lambda_{\text{em}} = 520$  nm, Bio-Rad, Japan), a 30 min incubation in darkness at room temperature, and a final two rinses in PBS. Stained samples were imaged using a fluorescence microscope (BZ-X700, Keyence, Japan). Obtained fluorescence micrographs were analyzed using commercially available software (Fiji, Fiji contributors).<sup>56,57</sup> Integrated intensities for both fluorophores were calculated from each sample's representative image. An additional sample from each condition was rinsed in PBS, dried, and then imaged using an SEM as described in section "SiYALON Glaze Characterization."

## RESULTS

### SiYALON glaze characterization

The SEM images of Figure 2 depict Si<sub>3</sub>N<sub>4</sub> sample surfaces coated with the SiYALON slurry before and after firing.

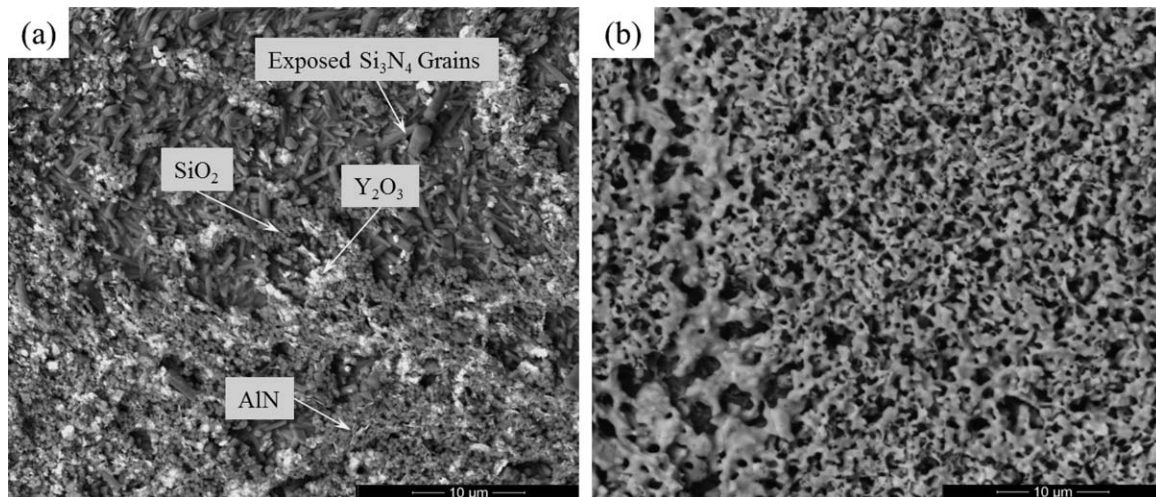


**FIGURE 2.** Back-scattered electron micrographs of as-fabricated  $\text{Si}_3\text{N}_4$  surface following dip-coating with 0.25 vol % SiYAlON slurry and subsequent drying (a) prior to and (b) following annealing at  $1400^\circ\text{C}$  for 30 min in 1–2 psi  $\text{N}_2$ . Silica (dark spheres), yttria (light platelets), and aluminum nitride (light rods) particles along with exposed  $\text{Si}_3\text{N}_4$  substrate grains are indicated in (a).

Shown in in Figure 2(a) is the particulate coverage of the dip-coated and dried slurry. Under back-scatter imaging, contrasting light and dark areas within the image provide evidence of its multiphase nature.<sup>58</sup> Intermixed  $\text{SiO}_2$  spheres,  $\text{Y}_2\text{O}_3$  platelets, and AlN needles were all visible. Less conspicuous were the  $\theta\text{-Al}_2\text{O}_3$  and  $\text{Si}_3\text{N}_4$  particles, which were present in the SiYAlON slurry at much lower concentrations than the other constituents. Figure 2(b) shows this sample subsequent to the glazing heat-treatment. The resultant glaze was uniform in surface coverage but highly textured and discontinuous. Evidence of liquid phase formation, likely the result of a low melting point eutectic between two or more of the constituents, and foaming were also observed. The glaze exhibited fine ( $\sim 100$  nm to  $1\ \mu\text{m}$ ) open porosity, and a higher average atomic weight (based on the increase in back-scattered electron intensity) than for  $\text{Si}_3\text{N}_4$  substrate. Minimal back-scatter image contrast within the glaze also indicated significant migration, mixing, and reaction of the constituent particles during the heat treatment cycle.

Provided in Table II are XPS data for the surface compositions of the AFSN,  $\text{N}_2$ ASN, and SiYAlON glazed samples. The presented data have carbon removed ( $<10\%$  in all cases) to allow for direct comparison of specific elements from one sample to another. As expected, the yttrium and aluminum content of the SiYAlON glazed sample and its Si:N:O ratio were significantly different from the AFSN and  $\text{N}_2$ ASN samples.

Figure 3(a) shows overlays of the XRD spectra from  $20^\circ$  to  $55^\circ$   $2\theta$  obtained from the AFSN and  $\text{N}_2$ ASN controls in addition to the SiYAlON glazed sample. All three patterns were effectively identical at diffraction angles  $>55^\circ$  and exhibited only peaks consistent with  $\beta\text{-Si}_3\text{N}_4$  (per JCPDS 33–1160). Peaks not present in the AFSN  $\text{Si}_3\text{N}_4$  control (that is, presumed to be indicative of the glaze composition) were identified and matched to a majority phase of hexagonal N-apatite ( $\text{Y}_5\text{Si}_3\text{O}_{12}\text{N}$ , JCPDS 48–1625) and a minority

phase of monoclinic yttrium silicate ( $\text{Y}_2\text{SiO}_5$ , JCPDS 36–1476) at the surface of the  $\text{N}_2$ ASN control sample. N-apatite was also the majority phase in the SiYAlON glaze along with a minority amount of yttrium aluminum garnet (YAG, JCPDS 73–3184) and possible residual  $\text{SiO}_2$  in the form of cristobalite (JCPDS 76–1625). An additional unidentified peak at  $\sim 42.5^\circ$   $2\theta$  with similar shape and intensity was present in all three patterns.

Figure 3(b) shows the Raman spectra collected on the surfaces of the different  $\text{Si}_3\text{N}_4$  samples in the  $150\text{--}250\ \text{cm}^{-1}$  region. The spectra for the control samples were very similar and were deconvoluted into three bands at  $\sim 186$ ,  $210$ , and  $224\ \text{cm}^{-1}$ . The most striking feature in the Raman analysis was that the SiYAlON glazed sample exhibited similar bands at  $186$  and  $210\ \text{cm}^{-1}$  in addition to bands at  $160$ ,  $188$ ,  $221$ , and  $229\ \text{cm}^{-1}$ .

#### Immersion in SBF

Representative micrographs of samples prior to SBF exposure are shown in Figure 4(a–c) for the AFSN and  $\text{N}_2$ ASN control samples, and for the SiYAlON glaze, respectively.

**TABLE II. Surface Elemental Composition via XPS for the As-Fabricated Surface Without Further Treatment, Following Exposure to  $1400^\circ\text{C}$  for 30 min in 1–2 psi  $\text{N}_2$ , and Following Dip Coating in 0.25 vol % SiYAlON Slurry and Subsequent Exposure to  $1400^\circ\text{C}$  for 30 min in 1–2 psi  $\text{N}_2$**

Element	As-Fabricated (AFSN)	$\text{N}_2$ -Annealed ( $\text{N}_2$ ASN)	SiYAlON Glazed
Si	38.9%	36.4%	28.1%
Y	0.1%	2.3%	10.9%
Al	2.3%	5.7%	3.4%
O	19.4%	18.5%	33.1%
N	39.3%	37.1%	24.6%

Carbon (4–10% for all samples) was removed to allow for direct comparison of other constituents. The  $\text{Si}_3\text{N}_4$  material's theoretical bulk composition is included for reference.

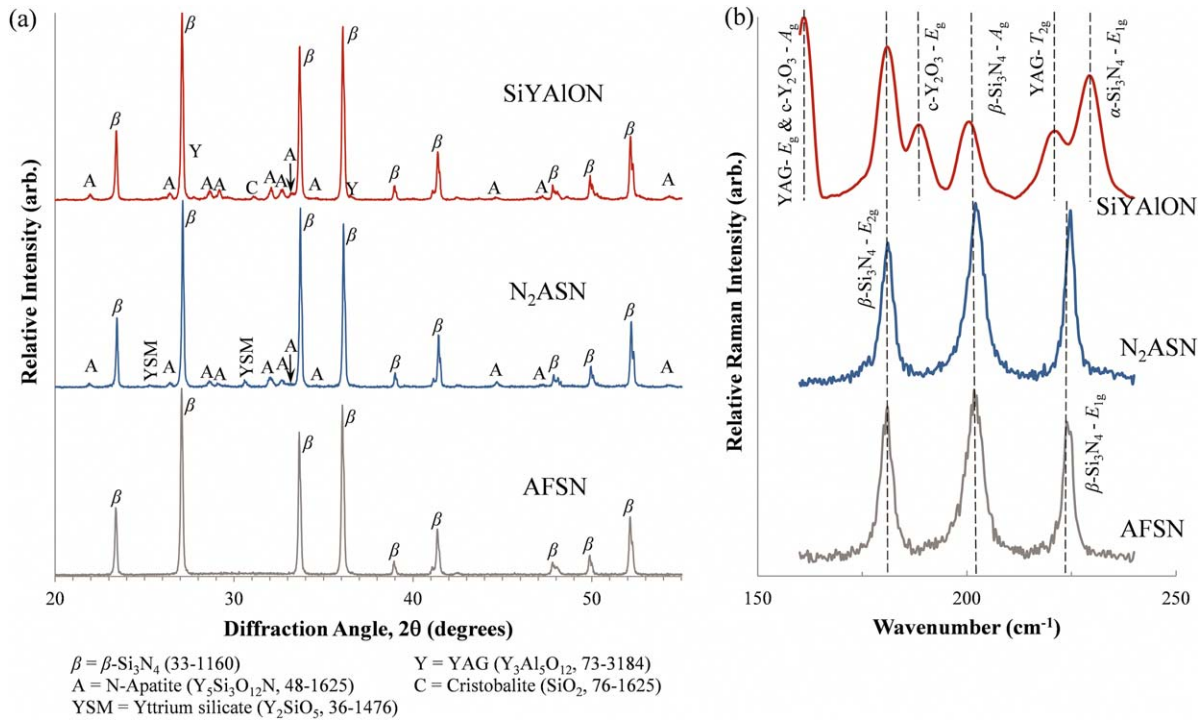


FIGURE 3. (a) Representative XRD patterns and (b) Raman spectra obtained for AFSN, N<sub>2</sub>ASN, and SiYAION glazed samples.

These same samples are respectively shown again after exposure to SBF in Figure 4(d–f). In the cases of AFSN and N<sub>2</sub>ASN control samples, a fine deposition layer was observed on the grain surfaces. However, for the SiYAION glazed sample, regions of thicker deposition are clearly visible. Further, as illustrated in Figure 4(g), larger islands of material rich in the constituents of biomimetic HAP were also deposited on the SiYAION glazed surface. Using XPS data obtained prior to and following the SBF immersion experiment, a graph displayed in Figure 4(h), correlates the observed postimmersion surface concentration of calcium plus phosphorus with the substrate surface concentration of aluminum plus yttrium relative to all cations (a proxy for SiYAION surface coverage) prior to immersion. A simple linear interpolation demonstrates that the deposition of Ca and P is directly proportional to SiYAION surface coverage.

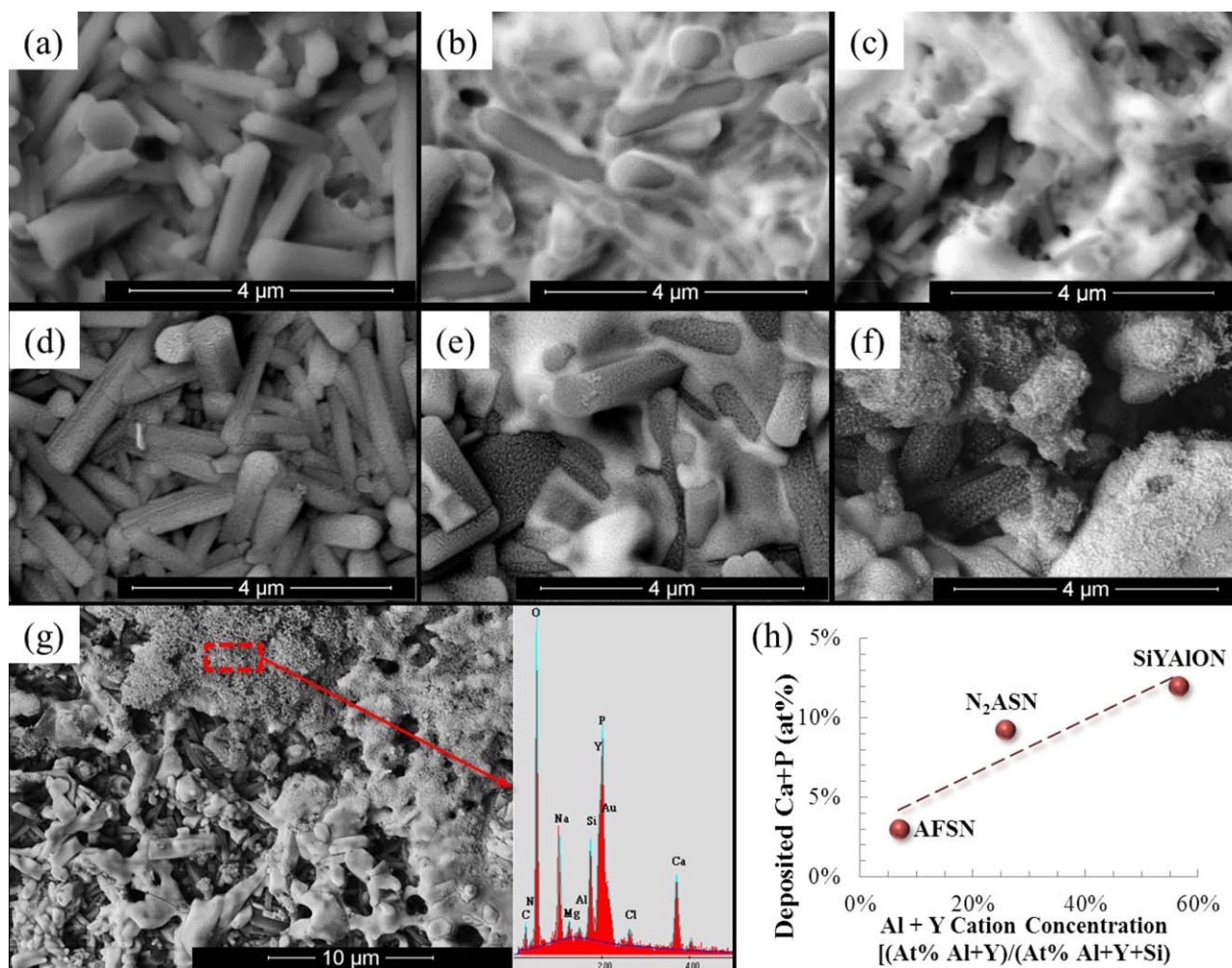
#### In vitro osteosarcoma exposure

Figure 5(a–c) provides Raman image maps generated for treated Si<sub>3</sub>N<sub>4</sub> surfaces exposed to Saos-2 cell cultures in an osteogenic medium for a period of 7 days. The major band for P–O stretching within PO<sub>4</sub><sup>3-</sup> tetrahedra (965 ± 12.5 cm<sup>-1</sup>) of HAP is intensity-contrasted in red, and the major band for C–H stretching in collagen is intensity-contrasted in green (2939.5 ± 42.6 cm<sup>-1</sup>). In these images, the AFSN [Figure 5(a)] and N<sub>2</sub>ASN [Figure 5(b)] specimens appear to show similar collagen and HAP coverage. However, the SiYAION glazed sample [Figure 5(c)] showed significantly more surface coverage and more HAP deposition relative to the two controls. Figure 5(d) presents the Raman spectra, averaged over each sample's respective image map,

in the vicinity of the P–O stretching band within PO<sub>4</sub><sup>3-</sup> tetrahedra. The area under the peak, defined within the window of 965 ± 12.5 cm<sup>-1</sup>, is proportional to the volume of HAP within the sampled volume. Plotted in Figure 5(e) are each sample's average peak area (normalized to the AFSN sample) as a function of surface atomic percent of Y and Al (also normalized to total surface cation concentration by XPS). This graph approximates the relationship between the volume of deposited HAP and the degree of SiYAION coverage on the surface. A clear trend is evident demonstrating increased HAP deposition as SiYAION coverage increases.

Figure 6 shows fluorescence micrographs, capturing the 520 nm emission associated with osteocalcin, for (a) AFSN, (b) N<sub>2</sub>ASN, and (c) SiYAION, along with the 461 nm emission associated with DNA present within the osteosarcoma cell nuclei, for (d) AFSN, (e) N<sub>2</sub>ASN, and (f) SiYAION, at low magnification. Figure 6(g) is a chart that shows the emission intensity for each of the fluorophores at their respective emission wavelengths integrated over each sample's respective image and normalized by the largest integrated intensity within the sample group. Both treated samples show an approximate twofold increase in osteocalcin. The annealed sample shows a modest increase in nuclear density while the SiYAION-glazed sample shows a more than twofold increase in nuclear density relative to the as-fired sample.

Figure 7 shows backscatter SEM images after osteosarcoma exposure at (a, b and c) low and (d, e, and f) high magnification for AFSN, N<sub>2</sub>ASN, and SiYAION, respectively. Low magnification images show the degree of surface coverage with ECP and the distribution of mineralized nodule clusters. High magnification images show details of



**FIGURE 4.** Back-scattered electron micrographs of AFSN, N<sub>2</sub>ASN, and SiYAION glazed samples (a, b, and c, respectively) prior to and (d, e, and f, respectively) following immersion in SBF for 28 days. (g) Island of deposited HAp (presumed) with accompanying EDS spectrum on SiYAION glazed surface, and (h) Chart of at% Ca + P deposited during SBF immersion as a function of Al + Y surface cation concentration, normalized by total cation concentration, via XPS.

mineralized nodule clusters. EDS spectra are inset into high magnification images to show qualitative atomic compositions of mineralized nodules, which are consistent with a mixture of native HAP and ECP.

## DISCUSSION

### SiYAION glaze characterization

It was hypothesized that a thin layer of material with a composition mimicking that of the IGP could be applied to the Si<sub>3</sub>N<sub>4</sub> surface via a glazing approach. This was demonstrated by applying a dilute slurry containing submicron particles approximating the composition of the IGP to the material's surface followed by a subsequent heat treatment. As can be seen in Figure 2(a), the slurry dispersion was reasonably uniform, and mixing of the constituents was maintained throughout drying. Following the heat treatment, it is evident that reaction of the constituents with each other and the substrate occurred along with limited melting and foaming. Note that the significant amount of porosity seen within the glaze may be advantageous in enhancing

osseointegration by increasing the surface area available for charge-mediated and/or dissolution interactions between the medium and sample surface. The surface composition of the SiYAION glaze (cf. Table II) showed a significant increase in both yttrium and oxygen relative to the theoretical bulk, AFSN, and N<sub>2</sub>ASN control samples. This indicates that more of the underlying Si<sub>3</sub>N<sub>4</sub> substrate had been covered by the SiYAION mixture. A significant change in Al concentration at the surface was not expected since it was already present at ~3 at %. A similar concentration existed within the SiYAION glaze itself. Another key difference between the SiYAION glaze and the N<sub>2</sub>ASN control is the nitrogen to oxygen ratio (i.e., N:O). It is ~2:1 for the N<sub>2</sub>ASN sample and 2:1.5 for the SiYAION glazed sample, illustrating the increased SiYAION coverage on the glazed sample relative to the N<sub>2</sub>ASN sample.

The XRD data presented in Figure 3(a) provide further evidence of differences in phase composition between the externally applied SiYAION glaze and the N<sub>2</sub>ASN surface SiYAION islands. In the N<sub>2</sub>ASN case, the majority phase was

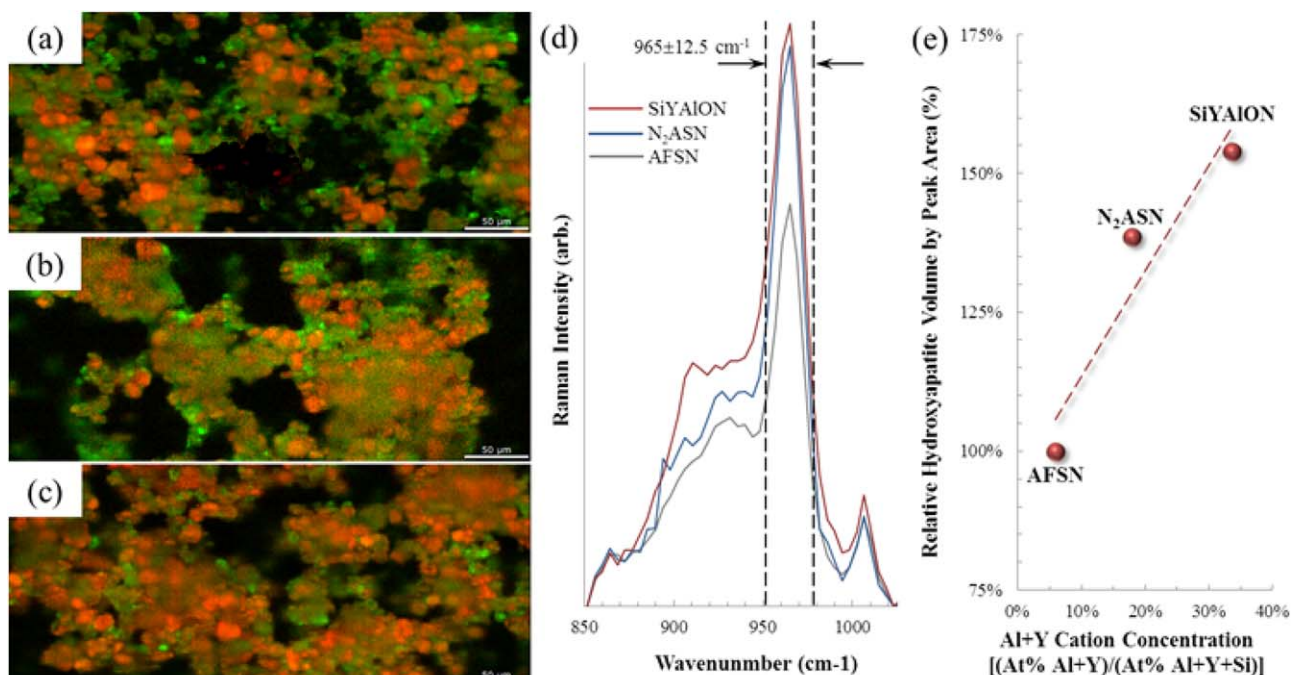


**FIGURE 5.** Raman intensity maps showing representative surface coverage of HAp (red scale, Raman shift  $965 \pm 12.5 \text{ cm}^{-1}$ ) and collagen (green scale, Raman shift  $2939.5 \pm 42.6 \text{ cm}^{-1}$ ) following osteosarcoma exposure to (a) AFSN, (b) N<sub>2</sub>ASN, and (c) SiYAION glazed samples. (d) Averaged Raman spectra (in region of at  $965 \pm 12.5 \text{ cm}^{-1}$ ) and (e) area under curve at  $965 \pm 12.5 \text{ cm}^{-1}$ , normalized by the AFSN sample's value, as a function of Al + Y surface cation concentration, normalized by total cation concentration, via XPS.

identified as nitrogen-apatite ( $\text{Y}_5\text{Si}_3\text{O}_{12}\text{N}$ ), with a minority phase of monoclinic yttrium silicate ( $\text{Y}_2\text{SiO}_5$ ). Nitrogen apatite was also present as the majority phase within the spectrum of the SiYAION glaze. However, in lieu of a minority yttrium silicate constituent, yttrium aluminum garnet (YAG,  $\text{Y}_3\text{Al}_5\text{O}_{12}$ ) and cristobalite ( $\text{SiO}_2$ ) were identified minority constituents. Formation of these phases from the original slurry constituents ( $\text{Y}_2\text{O}_3$ ,  $\text{SiO}_2$ ,  $\text{Al}_2\text{O}_3$ ,  $\text{Si}_3\text{N}_4$ , and  $\text{AlN}$ ) was not surprising and indicates that while the SiYAION glaze was similar in composition to the IGP, it was not an exact replicate. Furthermore, the SiYAION mixture was only exposed to  $1400^\circ\text{C}$ , which is significantly lower than  $\sim 1700^\circ\text{C}$  where the IGP is initially formed. In addition to differences in surface coverage, the presence of these phases also accounts for the observed variation in N:O ratios between the N<sub>2</sub>ASN and SiYAION samples. Since the unidentified minority peak at  $\sim 42.5^\circ 2\theta$  exhibited similar shape and intensity across all three sample spectra, it was assumed to correspond to a substrate constituent.

Analysis of Raman spectra further confirmed the polyphasic nature of the SiYAION glaze. In Figure 3(b), three bands in the Raman spectra located at  $180.1$ ,  $201.4$ , and  $224.5 \text{ cm}^{-1}$  for all samples represent the  $E_{2g}$ ,  $A_g$ , and  $E_{1g}$  vibrational modes of the skeletal Si—N bonds in the  $\beta$ - $\text{Si}_3\text{N}_4$  crystal, respectively.<sup>59,60</sup> In the case of the SiYAION sample, the  $E_{1g}$  band is possibly present but obscured by nearby bands at  $221$  and  $229 \text{ cm}^{-1}$ . In addition, present in this sample's spectrum were two additional bands at  $161$  and  $188 \text{ cm}^{-1}$ . The bands at  $161$  and  $221 \text{ cm}^{-1}$  correspond to the  $E_g$  and  $T_{2g}$  bands from YAG<sup>61–63</sup> and the band at  $188 \text{ cm}^{-1}$  may correspond to the  $E_g$  band from cubic yttrium oxide,<sup>64,65</sup> which

also exhibits a band for the  $A_g$  vibrational mode at  $161 \text{ cm}^{-1}$ . The  $229 \text{ cm}^{-1}$  band may correspond to the  $E_{1g}$  band of  $\alpha$ - $\text{Si}_3\text{N}_4$ ,<sup>66</sup> left as an unreacted remnant within the glazing slurry due to the treatment temperature being lower than required for inducing a transformation to the  $\beta$  phase. The YAG result complements the XRD spectrum obtained for this sample, which exhibited peaks at locations common to YAG standards. Given that yttria is a majority constituent of the glaze mixture, the presence of an unreacted remnant was not unexpected. The lack of non-substrate bands in the N<sub>2</sub>ASN sample's spectrum is thought to be due to lower coverage and thickness of the expressed IGP at the surface relative to the SiYAION glazed sample.

#### Immersion in SBF

Sample surfaces prior to SBF immersion are imaged in back-scatter mode in Figure 4(a–c). Stochastically protruding  $\beta$ - $\text{Si}_3\text{N}_4$  grains with smooth surfaces were observed on all samples and SiYAION material was intermixed with and coating these grains to varying degrees in the N<sub>2</sub>ASN and SiYAION glazed cases [compare Figure 4(b,c), respectively]. These same surfaces are shown following 30 days of SBF immersion in Figure 5(d–f). In all three cases, a thin, grainy deposition layer was observed. For the AFSN and N<sub>2</sub>ASN control sample, a thin layer of deposition is visible. Unfortunately, this grainy layer was not thick enough to successfully employ EDS for composition determination. In contrast, additional large, thick islands of this material, whose EDS spectrum is suggestive of biomimetic HAp, were clearly visible across the surface of the SiYAION glazed sample

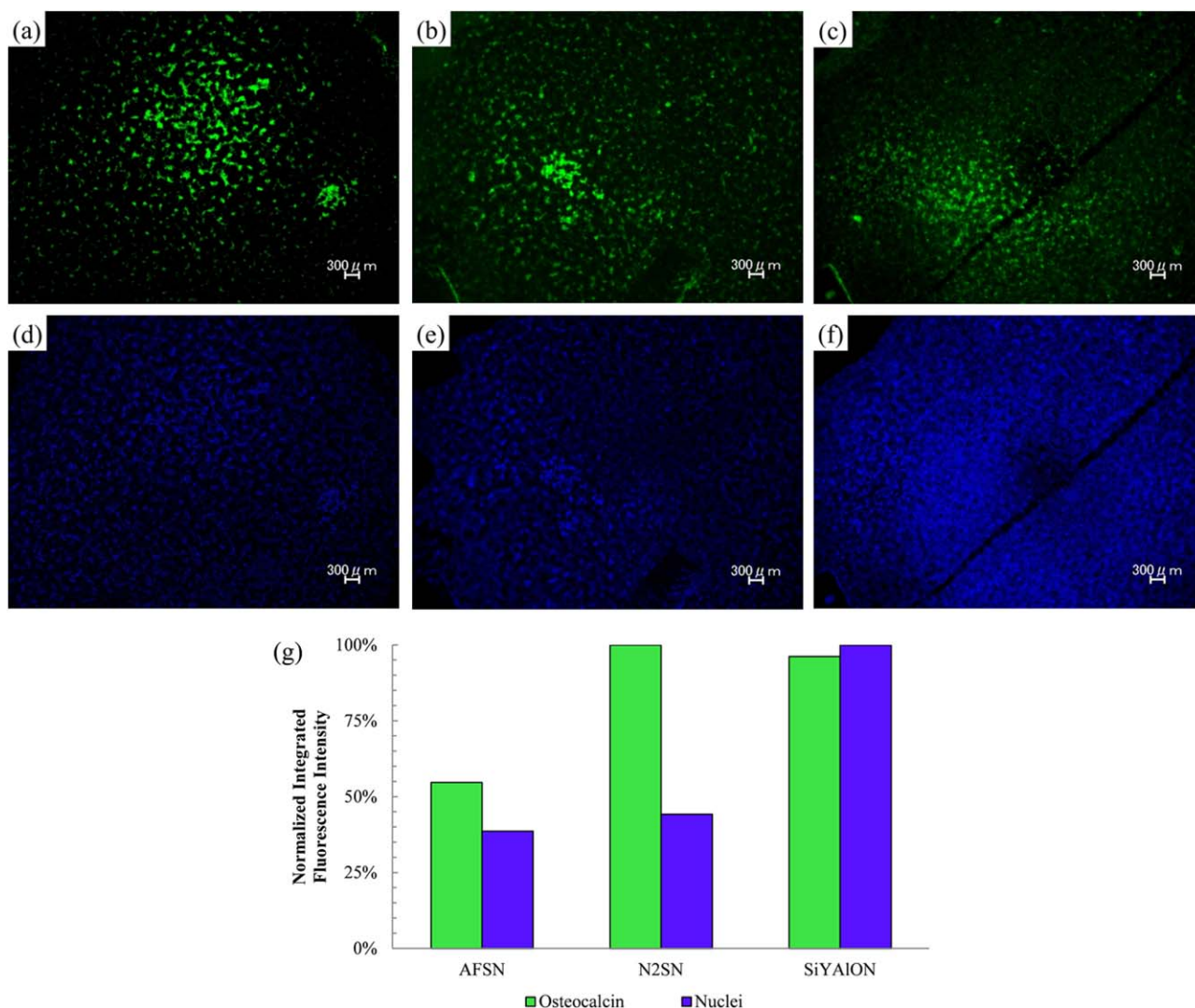


**FIGURE 6.** Fluorescence micrographs showing emission at 520 nm for antibody bound to osteocalcin on (a) AFSN, (b) N<sub>2</sub>ASN, and (c) SiYAION surfaces following 7 day osteosarcoma culture exposure. Fluorescence micrographs of emission at 461 nm showing the location of DNA in cell nuclei on (d) AFSN, (e) N<sub>2</sub>ASN, and (f) SiYAION surfaces following 7 day osteosarcoma culture exposure. (g) Normalized integrated fluorescence intensities for osteocalcin and DNA in cell nuclei for each specimen.

[compare Figure 5(g)]. These islands also appear to morphologically conform to deposited HAp previously observed by others during similar experiments.<sup>47,49,67–69</sup> XPS was employed to determine the elemental composition of the observed grainy layers. They were found to be rich in Ca and P along with minority amounts of Na, Mg, Cl, and C, consistent with biomimetic HAp or its precursors. The graph in Figure 5(h) shows surface at.% Ca plus P following SBF immersion as a function of pre-immersion Al plus Y (normalized by total cation concentration). This graphical comparison suggests that deposition of HAp-like material increases as a function of SiYAION glaze surface coverage.

#### ***In vitro* osteosarcoma cell exposure**

Representative Raman spectra for each sample type following 7-days of Saos-2 cell exposure are provided in Figure 5(a–c). The green-contrasted regions indicate deposition of

collagen, the primary component of the Saos-2 cells' extracellular matrix. Observation of collagen deposition illustrates the extent to which the Saos-2 cells have spread out on the sample surface and formed a pseudo-osteoid. The red-contrasted regions are areas where HAp has been deposited onto the pseudo-osteoid. The AFSN [Figure 5(a)] and N<sub>2</sub>ASN [Figure 5(b)] control samples appeared to exhibit similar amounts of collagen coverage and mineralization. However, the SiYAION glazed sample [Figure 5(c)] exhibited both significantly more collagen coverage and HAp deposition. Figure 5(d) shows the averaged Raman spectra, centered at  $\sim 960\text{ cm}^{-1}$  for P–O stretching within HAp  $\text{PO}_4^{3-}$  tetrahedra, for each of these samples. A large increase in intensity and peak area was observed for the N<sub>2</sub>ASN sample relative to the AFSN material, indicating substantially more matrix mineralization. However, even further increased band intensity and peak area were observed for the SiYAION glazed

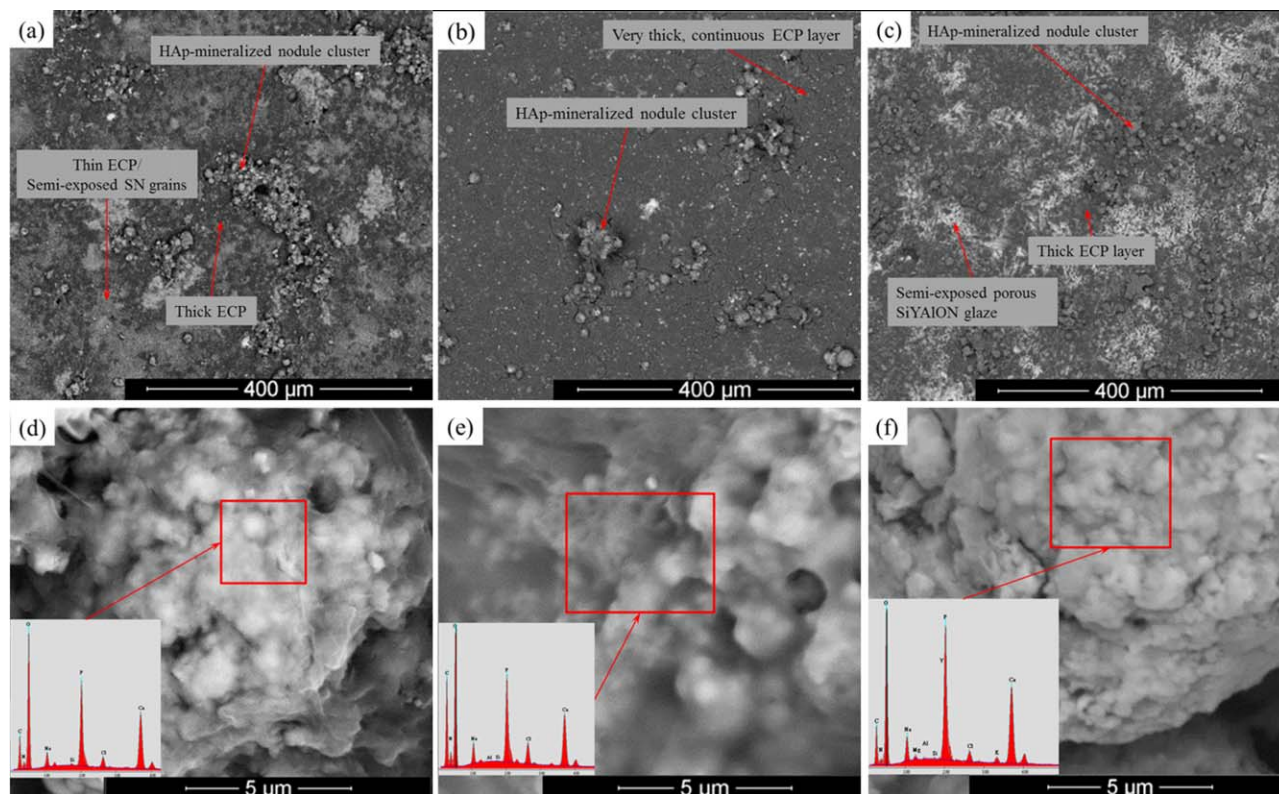


**FIGURE 7.** Low magnification backscatter SEM images of (a) AFSN, (b)  $N_2$ ASN, and (c) SiYAION surfaces following 7 day osteosarcoma culture exposure. High magnification images of mineralized nodules with EDS spectra inset on (d) AFSN, (e)  $N_2$ ASN, and (f) SiYAION surfaces following 7 day osteosarcoma culture exposure.

sample. Sample peak area, normalized by the AFSN sample's peak area, was charted as a function of surface atomic percent aluminum plus yttrium, normalized by total surface cation content in Figure 5(e). This relationship is a proxy for volume of deposited HAp as a function of SiYAION phase surface coverage. This graph demonstrates a trend of enhanced mineralization as a function of increasing SiYAION coverage.

All three conditions show expression of osteocalcin [Figure 6(a-c)], which provides evidence of cell-mediated matrix mineralization and increased cell activity.<sup>70</sup> Osteocalcin is present at approximately double the concentration on both treated samples relative to the as-fired sample [Figure 6(g)]. DNA staining indicates spreading of cell nuclei across all three sample surfaces [Figure 6(d-f)]. In the case of  $N_2$ ASN [Figure 6(e)], there is a moderate increase in overall cell density that corresponds to sporadic clustering at higher density relative to the AFSN sample [Figure 6(d)]. In the case of the SiYAION-glazed sample [Figure 6(f)], the difference is dramatic with more than double the emission intensity [Figure 6(g)] relative to AFSN and large regions of higher density clustering.

Backscattered electron micrographs at low magnification [Figure 7(a-c)] illustrate the degree of surface coverage and the morphology of deposited material for each sample condition. Patterns of deposited material correspond to patterns observed in fluorescence micrographs (Figure 6) for

osteocalcin and cell nuclei. Approximately half of the AFSN [Figure 7(a)] surface is covered in a connective web of ECP (dark material) with islands of mineralized nodular clusters (light material) typically separated from one another by  $\sim 200 \mu\text{m}$ . The medium gray material is semi-exposed  $\text{Si}_3\text{N}_4$  which is coated by a thin layer of ECP. The ECP itself is sporadically covered by fine mineral precipitates. These are potentially heterogeneous nucleation sites due to their distance from the nodular clusters. The  $N_2$ ASN sample [Figure 7(b)] shows nearly complete coverage in ECP (dark material) with mineralized nodular clusters that are spaced somewhat irregularly relative to the AFSN sample. Virtually none of the underlying material surface is visible. Finally, the SiYAION glaze sample [Figure 7(c)] shows  $\sim 65\%$  coverage by connective ECP (dark material) with mineralized nodular clusters (moderately lighter than ECP), spaced more closely to one another ( $\sim 100 \mu\text{m}$  apart) than on the other samples. Also visible are regions of semi-exposed porous SiYAION glaze (lightest). Higher magnification images and associated EDS patterns [Figure 7(d-f)] give a clear picture of nodule morphology and quantitative atomic composition. All mineralized nodules exhibit a spectrum consistent with mineralized bone: a mixture of ECP (rich in C) and defective HAp (Ca, P, and O with Na, Cl, Mg, K, and  $\text{HCO}_3^-$  impurities). Nodules on the AFSN sample [Figure 7(d)] are mineral rich, exhibiting a relatively high ratio of Ca, O, and O to C. The  $N_2$ ASN sample [Figure 7(e)] nodules are rich in

ECP as demonstrated by the high ratio of C to the primary mineral constituents, Ca, P, and O. Finally, the nodules on the SiYAlON glaze sample [Figure 7(f)] surface appear to exhibit a mineral-rich composition similar to those present on the AFSN sample.

Regarding the mechanism of Saos-2 cell adsorption, proliferation, and HAp mineralization, it has been previously shown that SiYAlON possesses a zwitterionic-like surface at physiologic pH due to intermixing of surface moieties exhibiting negative ( $\equiv\text{Si}-\text{O}^-$ ) and positive ( $=\text{Y}-\text{OH}_2^+$ ,  $=\text{Al}-\text{OH}_2^+$ ,  $\equiv\text{Si}-\text{NH}_3^+$ ) charges.<sup>6,29</sup> Surfaces engineered to exhibit zwitterionic character through grafting of polymers containing this functionality have also previously demonstrated extreme hydrophilicity due to their high degree of surface polarization.<sup>71-73</sup> Additionally, a titanium alloy modified by grafting of a zwitterionic-functionalized polymer exhibited increased HAp deposition<sup>73</sup> when subjected to a variant of Kokubo's<sup>35</sup> *in vitro* SBF immersion test. Materials that exhibit a high net negative surface charge,<sup>50</sup> such as high surface area silica<sup>38,39</sup> and  $\text{Si}_3\text{N}_4$ ,<sup>74</sup> have also demonstrated the ability to induce heterogeneous HAp precipitation from SBF due to elevated concentrations of  $\text{Ca}^{2+}$  ions within the counterion clouds that shroud their highly-charged surfaces in solution. Additionally, the presence of the N-apatite phase within the SiYAlON glaze, which is isostructural to native HAp, likely further facilitates HAp precipitation due to a reduced energy barrier for heterogeneous nucleation.<sup>75</sup> Finally, chemical interactions between the extracellular medium, biomaterial surface, and osteoprogenitor cells can influence osteoblast differentiation and metabolism, production of extracellular collagen, cell motility, production of matrix vesicles, and expression of molecules that regulate the bone remodeling process.<sup>76-79</sup> For example, a recent study found that when amorphous nitrogen-doped silicon oxide thin films (*i.e.*, materials chemically similar to SiYAlONs) were exposed to human periosteal cells, they generated higher volumes of biomimetically deposited HAp *in vitro*. The presence of nitrogen induced expression of osteogenic genes<sup>80</sup> and SOD1,<sup>81</sup> (*i.e.*, an anti-oxidant critical for cross-linked collagen formation).

## CONCLUSIONS

It was found that a process reminiscent of traditional white-ware glazing could be employed to apply a thin, adherent SiYAlON coating onto a  $\text{Si}_3\text{N}_4$  bioceramic surface. The resulting glaze was characterized morphologically and chemically using a number of microscopic and spectroscopic techniques, revealing that it was multiphasic in nature. The principle crystalline phase within the glaze was determined to be N-apatite,  $\text{Y}_5\text{Si}_3\text{O}_{12}\text{N}$ . An *in vitro* assessment demonstrated the propensity for all  $\text{Si}_3\text{N}_4$  surfaces to induce CaP deposition, increasing as a function of surface SiYAlON coverage and independent of the presence of bone-forming cells. When osteoblast-like Saos-2 cells were employed in a parallel *in vitro* experiment, the SiYAlON glazed surface demonstrated improved cell proliferation and osteoid mineralization relative to both uncoated  $\text{Si}_3\text{N}_4$  (AFSN) and

nitrogen-annealed ( $\text{N}_2$ ASN)  $\text{Si}_3\text{N}_4$  controls, which was once again correlated to the relative amounts of surface SiYAlON coverage. In addition to validating previous work demonstrating improved cell response to SiYAlON surfaces, the SiYAlON glaze offers a potential new bioactive material that can not only be applied as a glaze to  $\text{Si}_3\text{N}_4$ , but also be employed as a coating for a broad range of existing biomedical devices used in therapies for bone and tissue repair.

Future studies will use different coating techniques, varied glaze compositions and glazing temperatures, and production of glaze material monoliths to better understand the phase composition and structure of these newly discovered bioactive SiYAlON materials. Additional ongoing work will also focus on coating and infusing of substrates other than  $\text{Si}_3\text{N}_4$  with SiYAlON-type materials. Promising samples from these experiments will be subjected to *in vitro* and *in vivo* testing to characterize their interaction with the biologic medium and their ability to influence regrowth of bone and other tissue types.

## ACKNOWLEDGMENTS

The authors gratefully acknowledge Dr. Brian van Devenor of the University of Utah for performing XPS measurements and aiding in data analyses. This work made use of University of Utah shared facilities of the Micron Microscopy Suite sponsored by the College of Engineering, Health Sciences Center, Office of the Vice President for Research, and the Utah Science Technology and Research (USTAR) initiative of the State of Utah. The authors also acknowledge Mr. Garrett Meeks for facilitating the XRD experiments conducted at the Materials Characterization Lab, which is supported in part by the Department of Materials Science and Engineering at the University of Utah.

## DISCLOSURES

R. M. Bock, Bryan J. McEntire, and B. S. Bal are employees of Amedica Corporation, a silicon nitride orthopaedic device manufacturer. G. Pezzotti is a consultant of Amedica Corporation. None of the other authors have a financial or proprietary interest in the subject matter or materials discussed.

## REFERENCES

1. Rezwan K, Chen QZ, Blaker JJ, Boccaccini AR. Biodegradable and bioactive porous polymer/inorganic composite scaffolds for bone tissue engineering. *Biomaterials*. 2006;27:3413-3431.
2. Surmenev RA, Surmeneva MA, Ivanova AA. Significance of Calcium Phosphate Coatings for the Enhancement of New Bone Osteogenesis—A Review. *Acta Biomater* 2014;10:557-579.
3. Rahaman MN. Bioactive Ceramics and Glasses for Tissue Engineering. In: Boccaccini AR, editor. *Tissue Eng Using Ceram Polym*. New York: Woohed Publishing; 2014.
4. Gallo J, Kontinen YT, Goodman SB, Thyssen JP, Gibon E, Pajarinen J, Takakubo Y, Schalock P, Mackiewicz Z, Jansen E, Petrek M, Trebse R, Coer A, Takagi M. Aseptic Loosening of Total Hip Arthroplasty as a Result of Local Failure of Tissue Homeostasis. In: Fokter S, editor. *Recent Adv Arthroplast*. Rijeka, Croatia: InTech; 2012.
5. Bahraminasab M, Sahari BB, Edwards KL, Farahmand F, Arumugam M. Aseptic Loosening of Femoral Components – Materials Engineering and Design Considerations. *Mater Des* 2013;44:155-163.

6. Pezzotti G, McEntire B, Bock R, Boffelli M, Zhu W, Vitale E, Puppulin L, Adachi T, Yamamoto T, Kanamura N, Bal BS. Silicon Nitride: A Synthetic Mineral for Vertebrate Biology. *Sci Rep* 2016; 6:31717.
7. Rahaman MN, Yao A, Bal BS, Garino JP, Ries MD. Ceramics for Prosthetic Hip and Knee Joint Replacement. *J Am Ceram Soc* 2007;90:1965–1988.
8. Mazzocchi M, Bellosi A. On the possibility of silicon nitride as a ceramic for structural orthopaedic implants. Part I: processing, microstructure, mechanical properties, cytotoxicity. *J Mater Sci Mater Med* 2008;19:2881–2887.
9. Mazzocchi M, Gardini D, Traverso PL, Faga MG, Bellosi A. On the Possibility of Silicon Nitride as a Ceramic for Structural Orthopaedic Implants. Part II: Chemical Stability and Wear Resistance in Body Environment. *J Mater Sci Mater Med* 2008;19:2889–2901.
10. Bal BS, Rahaman MN. Orthopedic Applications of Silicon Nitride Ceramics. *Acta Biomater* 2012;8:2889–2898.
11. Taylor RM, Bernero JP, Patel AA, Brodke DS, Khandkar AC. Silicon Nitride - A New Material for Spinal Implants. *J Bone Joint Surg* 2010;92-Br:133.
12. Lange FF. Relation Between Strength, Fracture Energy, and Microstructure of Hot-Pressed  $\text{Si}_3\text{N}_4$ . *J Am Ceram Soc* 1973;56:518–522.
13. Riley FL. Silicon Nitride and Related Materials. *J Am Ceram Soc* 2000;83:245–265.
14. Lange FF. The Sophistication of Ceramic Science Through Silicon Nitride Studies. *J Ceram Soc Jpn* 2006;114:873–879.
15. Becher PF, Sun EY, Plucknett KP, Alexander KB, Hsueh C, Lin H, Waters SB, Westmoreland CG. Microstructural Design of Silicon Nitride with Improved Fracture Toughness: I, Effects of Grain Shape and Size. *J Am Ceram Soc* 1998;81:2821–2830.
16. Bodišová K, Kašiarová M, Domanická M, Hnatko M, Lenčes Z, Nováková ZV, Vojtaššák J, Gromošová S, Šajgalík P. Porous silicon nitride ceramics designed for bone substitute applications. *Ceram Int* 2013;39:8355–8362.
17. Arts MP, Wolfs JFC, Corbin TP. The CASCADE Trial: Effectiveness of Ceramic Versus PEEK Cages for Anterior Cervical Discectomy with Interbody Fusion; Protocol of a Blinded Randomized Controlled Trial. *BMC Musculoskelet Disord* 2013;14:244.
18. Kersten RF, van Gaalen SM, Arts MP, Roes KCB, de Gast A, Corbin TP, Oner FC. The SNAP trial: A Double Blind Multi-Center Randomized Controlled Trial of a Silicon Nitride Versus a PEEK Cage in Transforaminal Lumbar Interbody Fusion in Patients with symptomatic degenerative lumbar disc disorders: study protocol. *BMC Musculoskelet Disord* 2014;15:57.
19. Kue R, Sohrabi A, Nagle D, Frondoza C, Hungerford D. Enhanced proliferation and osteocalcin production by human osteoblast-like MG63 cells on silicon nitride ceramic discs. *Biomaterials* 1999;20:1195–1201.
20. Howlett CR, McCartney E, Ching W. The Effect of Silicon Nitride Ceramic on Rabbit Skeletal Cells and Tissue. *Clin Orthop Relat Res* 1989;244:293–304.
21. Neumann A, Reske T, Held M, Jahnke K, Ragoss C, Maier HR. Comparative Investigation of the Biocompatibility of Various Silicon Nitride Ceramic Qualities in vitro. *J Mater Sci Mater Med* 2004;15:1135–1140.
22. Santos C, Ribeiro S, Daguano JKMF, Rogero SO, Strecker K, Silva CRM. Development and Cytotoxicity Evaluation of SiAlONs Ceramics. *Mater Sci Eng* 2007;27:148–153.
23. Sorrell CC, Hardcastle PH, Druitt RK, Howlett CR, McCartney ER. Results of 15-Year Clinical Study of Reaction Bonded Silicon Nitride Intervertebral Spacers. *Proc 7th World Biomater Conf* 2004;1872.
24. Neumann A, Kramps M, Ragoß C, Maier HR, Jahnke K. Histological and Microradiographic Appearances of Silicon Nitride and Aluminum Oxide in a Rabbit Femur Implantation Model. *Materwiss Werksttech* 2004;35:569–573.
25. Guedes-e-Silva CC, König B, Carbonari MJ, Yoshimoto M, Allegrini S, Bressiani JC. Tissue Response Around Silicon Nitride Implants in Rabbits. *J Biomed Mater Res* 2008;84A:337–343.
26. Anderson M, Bernero J, Brodke D. Medical Imaging Characteristics of Silicon Nitride Ceramic A New Material for Spinal Arthroplasty Implants. 8th Annu Spine Arthroplast Soc Glob Symp Motion Preserv Technol. Miami, FL; 2008.
27. Anderson MC, Olsen R. Bone ingrowth into porous silicon nitride. *J Biomed Mater Res* 2010;92:1598–1605.
28. Webster TJ, Patel AA, Rahaman MN, Bal BS. Anti-Infective and Osteointegration Properties of Silicon Nitride, Poly (Ether Ether Ketone), and Titanium Implants. *Acta Biomater* 2012;8:4447–4454.
29. Pezzotti G, McEntire BJ, Bock RM, Zhu W, Boschetto F, Rondinella A, Marin E, Marunaka Y, Adachi T, Yamamoto T, Kanamura N, Bal BS. In Situ Spectroscopic Screening of Osteosarcoma Living Cells on Stoichiometry-Modulated Silicon Nitride Bioceramic Surfaces. *ACS Biomater Sci Eng* 2016;2:1121–1134.
30. Pezzotti G, Bock RM, McEntire BJ, Jones E, Boffelli M, Zhu W, Baggio G, Boschetto F, Puppulin L, Adachi T, Yamamoto T, Kanamura N, Marunaka Y, Bal BS. Silicon Nitride Bioceramics Induce Chemically Driven Lysis in *Porphyromonas Gingivalis*. *Langmuir. Am Chem Soc* 2016;32:3024–3035.
31. Gorth DJ, Puckett S, Ercan B, Webster TJ, Rahaman M, Bal BS. Decreased Bacteria Activity on  $\text{Si}_3\text{N}_4$  Surfaces Compared with PEEK or Titanium. *Int J Nanomed* 2012;7:4829–4840.
32. Samaroo HD, Lu J, Webster TJ. Enhanced endothelial cell density on NiTi surfaces with sub-micron to nanometer roughness. *Int J Nanomed* 2008;3:75–82.
33. Personal Communication from William Jordan, Director of Regulatory Affairs and Quality Assurance, Amedica Corporation, Salt Lake City, UT 84119; 2016.
34. Bock RM, McEntire BJ, Bal BS, Rahaman MN, Boffelli M, Pezzotti G. Surface modulation of silicon nitride ceramics for orthopaedic applications. *Acta Biomater* 2015;26:318–330.
35. ISO 23317:2012(E). Implants for Surgery-In vitro Evaluation for Apatite-Forming Ability of Implant Materials; 2007.
36. McEntire BJ, Lakshminarayanan R, Thirugnanasambandam P, Seitz-Sampson J, Bock R, O'Brien D. Processing and Characterization of Silicon Nitride Bioceramics. *Bioceram Dev Appl* 2016;6:1–9.
37. Fair GE, Lange FF. Effect of Interparticle Potential on Forming Solid, Spherical Agglomerates during Drying. *J Am Ceram Soc* 2004;9:4–9.
38. Li P, Ohtsuki C, Kokubo T, Nakanishi K, Soga N, Nakamura T, Yamamoto T. Apatite Formation Induced on Silica Gel in a Simulated Body Fluid. *J Am Ceram Soc* 1992;75:2094–2097.
39. Li P, Ohtsuki JC, Kokubo T, Nakanishi K, Soga N, Groot K. De. The role of hydrated silica, titania, and alumina in inducing apatite on implants. *J Biomed Mater Res* 1994;28:7–15.
40. Kokubo T. Apatite Formation on Surfaces of Ceramics, Metals and Polymers in Body Environment. *Acta Mater* 1998;46:2519–2527.
41. Takadama H, Kim H, Kokubo T, Nakamura T. An X-ray photoelectron spectroscopy study of the process of apatite formation on bioactive titanium metal. *J Biomed Mater Res* 2001;55:185–193.
42. Takadama H, Kim H, Kokubo T, Nakamura T. TEM-EDX study of mechanism of bonelike apatite formation on bioactive titanium metal in simulated body fluid. *J Biomed Mater Res* 2001;57:441–448.
43. Ohtsuki C, Kokubo T, Yamamoto T. Mechanism of Bonelike Apatite Formation on Bioactive Tantalum Metal in a Simulated Body Fluid. *Biomaterials* 2002;23:827–832.
44. Oyane A, Onuma K, Ito A, Kim H, Kokubo T, Nakamura T. Formation and growth of clusters in conventional and new kinds of simulated body fluids. *J Biomed Mater Res A* 2003;64:339–348.
45. Kokubo T, Hanakawa M, Kawashita M, Minoda M, Beppu T, Miyamoto T, Nakamura T. Apatite formation on non-woven fabric of carboxymethylated chitin in SBF. *Biomaterials* 2004;25:4485–4488.
46. Kokubo T. Design of bioactive bone substitutes based on biomineralization process. *Mater Sci Eng C* 2005;25:97–104.
47. Kokubo T, Matsushita T, Takadama H, Kizuki T. Development of bioactive materials based on surface chemistry. *J Eur Ceram Soc* 2009;29:1267–1274.
48. Kim H, Himeno T, Kawashita M, Lee J, Kokubo T, Nakamura T. Surface potential change in bioactive titanium metal during the process of apatite formation in simulated body fluid. *J Biomed Mater Res A* 2003;67:1305–1309.
49. Fujibayashi S, Neo M, Kim H-M, Kokubo T, Nakamura T. A Comparative Study Between in vivo Bone Ingrowth and in vitro

- Apatite Formation on Na<sub>2</sub>O-CaO-SiO<sub>2</sub> Glasses. *Biomaterials* 2003; 24:1349–1356.
50. Kokubo T, Takadama H. How useful is SBF in predicting in vivo bone bioactivity? *Biomaterials* 2006;27:2907–2915.
  51. Takemoto M, Fujibayashi S, Neo M, Suzuki J, Matsushita T, Kokubo T, Nakamura T. Osteoinductive porous titanium implants: effect of sodium removal by dilute HCl treatment. *Biomaterials* 2006;27:2682–2691.
  52. Kokubo T, Kim H, Kawashita M. Novel bioactive materials with different mechanical properties. *Biomaterials* 2003;24:2161–2175.
  53. Penel G, Delfosse C, Descamps M, Leroy G. Composition of Bone and Apatitic Biomaterials as Revealed by Intravital Raman Microspectroscopy. *Bone* 2016;36:893–901.
  54. Mandair GS, Morris MD. Contributions of Raman spectroscopy to the understanding of bone strength. *Bonekey Rep* 2015;4:620.
  55. McQuillan DJ, Richardson MD, Bateman JF. Matrix Deposition by a Calcifying Human Osteogenic Sarcoma Cell Line (SAOS-2). *Bone* 1995;16:415–426.
  56. Schindelin J, Arganda-Carreras I, Frise E, Kaynig V, Longair M, Pietzsch T, Preibisch S, Rueden C, Saalfeld S, Schmid B, Tinevez J-Y, White DJ, Hartenstein V, Eliceiri K, Tomancak P, Cardona A. Fiji: an open-source platform for biological-image analysis. *Nat Methods* 2012;9:676–682.
  57. Schindelin J, Rueden CT, Hiner MC, Eliceiri KW. The ImageJ ecosystem: An open platform for biomedical image analysis. *Mol Reprod Dev* 2015;82:518–529.
  58. Goldstein J, Newbury DE, Joy DC, Lyman CE, Echlin P, Lifshin E, Sawyer L, Michael JR. *Scanning Electron Microscopy and X-Ray Microanalysis*, 3rd ed. New York: Springer Science & Business Media; 2003.
  59. Honda K, Yokoyama S, Tanaka S. Assignment of the Raman Active Vibration Modes of  $\beta$ -Si<sub>3</sub>N<sub>4</sub> using Micro-Raman Scattering. *J Appl Phys* 1999;85:7380–7384.
  60. Sato Y, Motoi S. Studies of the State of Iron Contained in  $\alpha$ - and  $\beta$ -Silicon Nitride by Mössbauer and Raman Effects. *J Phys Chem Solids* 1979;40:1–7.
  61. Chiriu D, Ricci PC, Carbonaro CM, Anedda A, Aburish-Hmidat M, Grosu A, Lorrai PG, Fortin E. Vibrational Properties of Mixed (Y<sub>3</sub>Al<sub>5</sub>O<sub>12</sub>)<sub>x</sub>(Y<sub>3</sub>Sc<sub>2</sub>Ga<sub>3</sub>O<sub>12</sub>)<sub>1-x</sub> crystals. *J Appl Phys* 2006;100:33101.
  62. Lukowiak A, Wiglusz RJ, MacZka M, Gluchowski P, Strek W. IR and Raman spectroscopy study of YAG nanoceramics. *Chem Phys Lett* 2010;494:279–283.
  63. Lu J, Ueda K, Yagi H, Yanagitani T, Akiyama Y, Kaminskii AA. Neodymium doped yttrium aluminum garnet (Y<sub>3</sub>Al<sub>5</sub>O<sub>12</sub>) nanocrystalline ceramics—a new generation of solid state laser and optical materials. *J Alloys Compd* 2002;341:220–225.
  64. Repelin Y, Proust C, Husson E, Beny JM. Vibrational Spectroscopy of the C-Form of Yttrium Sesquioxide. *J Solid State Chem* 1995;118:163–169.
  65. Husson E, Proust C, Gillet P, Itié JP. Phase Transitions in Yttrium Oxide at High Pressure Studied by Raman Spectroscopy. *Mater Res Bull* 1999;34:2085–2092.
  66. Wada N, Solin SA, Wong J, Prochazka S, Lansing E. Raman and IR absorption spectroscopic studies on  $\alpha$ ,  $\beta$ , and amorphous Si<sub>3</sub>N<sub>4</sub>. *J Non Cryst Solids* 1981;43:7–15.
  67. Jalota S, Bhaduri SB, Tas AC. Effect of carbonate content and buffer type on calcium phosphate formation in SBF solutions. *J Mater Sci Mater Med* 2006;17:697–707.
  68. Cüneyt Tas A. Synthesis of Biomimetic Ca-Hydroxyapatite Powders at 37°C in Synthetic Body Fluids. *Biomaterials* 2000;21:1429–1438.
  69. Zhu P, Masuda Y, Koumoto K. The effect of surface charge on hydroxyapatite nucleation. *Biomaterials*. 2004;25:3915–3921.
  70. Stein GS, Lian JB, Owen TA. Relationship of cell growth to the regulation of tissue-specific gene expression during osteoblast differentiation. *FASEB J* 1990;4:3111–3123.
  71. Schlenoff JB. Zwitteration: Coating Surfaces with Zwitterionic Functionality to Reduce Nonspecific Adsorption. *Langmuir* 2014; 30:9625–9636.
  72. Sin MC, Sun YM, Chang Y. Zwitterionic-based stainless steel with well-defined polysulfobetaine brushes for general bioadhesive control. *ACS Appl Mater Interfaces* 2014;6:861–873.
  73. Liu P, Domingue E, Ayers DC, Song J. Modification of Ti6Al4V Substrates with Well-defined Zwitterionic Polysulfobetaine Brushes for Improved Surface Mineralization. *ACS Appl Mater Interfaces* 2014;6:7141–7152.
  74. Precnerová M, Bodišová K, Frajkorová F, Galusková D, Varchulová Nováková Z, Vojtaššák J, Lenčes Z, Šajgalík P. In vitro Bioactivity of Silicon Nitride – Hydroxyapatite Composites. *Ceram Int* 2015;41:8100–8108.
  75. Combes C, Cazalbou S, Rey C. Apatite Biominerals. *Minerals. Multidisciplinary Digital Publishing Institute* 2016;6:34.
  76. Fedde KH. Human osteosarcoma cells spontaneously release matrix-vesicle-like structures with the capacity to mineralize. *Bone Miner* 1992;17:145–151.
  77. Anderson HC. Molecular Biology of Matrix Vesicles. *Clin Orthop Relat Res* 1995;266–280.
  78. Anderson HC. Matrix vesicles and calcification. *Curr Rheumatol Rep* 2003;5:222–226.
  79. Golub EE. Role of Matrix Vesicles in Biomineralization. *Biochim Biophys Acta* 2009;1790:1592–1598.
  80. Ilyas A, Lavrik N V., Kim HKW, Aswath PB, Varanasi VG. Enhanced Interfacial Adhesion and Osteogenesis for Rapid “bone-like” Biomineralization by PECVD-Based Silicon Oxynitride Overlays. *ACS Appl Mater Interfaces* 2015;7:15368–15379.
  81. Ilyas A, Odatsu T, Shah A, Monte F, Kim HKW, Kramer P, Aswath PB, Varanasi VG. Amorphous Silica: A New Antioxidant Role for Rapid Critical-Sized Bone Defect Healing. *Adv Healthc Mater* 2016; 5:2199–2213.